Journal of Power Sources 455 (2020) 227992

Contents lists available at ScienceDirect

Journal of Power Sources

journal homepage: www.elsevier.com/locate/jpowsour

Interweaving between MnO_2 nanowires/ nanorods and carbon nanotubes as robust multifunctional electrode for both liquid and flexible electrochemical energy devices

Nengneng Xu [a,c,1], Jiawen Liu [b,1], Jinli Qiao [a,*], Haitao Huang [d], Xiao-Dong Zhou [c,**]

[a] State Key Laboratory for Modification of Chemical Fibers and Polymer Materials, College of Environmental Science and Engineering, Donghua University, 2999 Ren'min North Road, Shanghai, 201620, China
[b] Shanghai Jinyuan Senior High School, 2169 Xincun Road, Shanghai, 200333, China
[c] Department of Chemical Engineering, University of Louisiana at Lafayette, Lafayette, LA, 70504, USA
[d] Department of Applied Physics, Hong Kong Polytechnic University, Hong Kong, China

HIGHLIGHTS

- The hybrid with interweaving structure between MnO_2 NWs/NRs and CNTs are designed.
- The MnO_2-NWRs/CNTs is evaluated for liquid/flexible ZABs, MABs, supercapacitors.
- The hybrid shows high electrochemical performances (ΔE: 0.98 V and 1183 F g^{-1}).
- The high performances of the hybrid are induced by its unique characteristics.

GRAPHICAL ABSTRACT

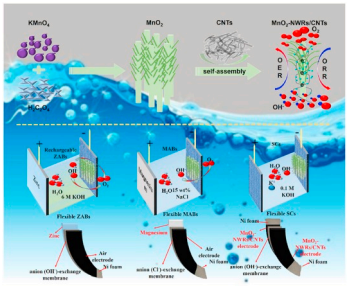

ARTICLE INFO

Keywords:
Multifunctional electrocatalyst
Flexible
Anion-exchange membrane
Metal-air batteries
Supercapacitors

ABSTRACT

In this paper, as a proof-of-concept study, a newly designed multifunctional composite electrode materials consisting of an interweaving structure of MnO_2 nanowires (NWs)/nanorods (NRs) and carbon nanotubes (CNTs) (MnO_2-NWRs/CNTs) are directly synthesized by a facile and scalable strategy, which show high catalytic activity for both oxygen reduction reaction (ORR)/oxygen evolution reaction (OER) processes and large specific capacitance for supercapacitors (SCs). Such a MnO_2-NWRs/$CNTs_{350}$ material is induced by the strong coupling and synergistic effect between MnO_2-NWRs and CNTs, as well as the coexistence of NRs/NWs and the existence of favorable crystal planes, which enable the multifunctional high-performance in zinc-air batteries (ZABs), magnesium-air batteries (MABs), SCs and also their flexible devices. The MnO_2-NWRs/$CNTs_{350}$ catalyst exhibits high electrochemical activity (ΔE: 0.98 V), decent capacitance (1183 F g^{-1}) and excellent battery performance (specifically, 640 mW cm^{-2} for MABs). In MnO_2-NWRs/$CNTs_{350}$, the (110) and (101) crystal planes of MnO_2-NWRs are advantageous for both ORR and OER processes. Additionally, the structural changes of MnO_2-NWRs/$CNTs_{350}$ (the coexistent NRs and NWs) improve the capacitance of the material. Even more encouraging, the

* Corresponding author.
** Corresponding author.
E-mail addresses: qiaojl@dhu.edu.cn (J. Qiao), xiao-dong.zhou@louisiana.edu (X.-D. Zhou).
[1] Nengneng Xu and Jiawen Liu contributed equally to this work.

https://doi.org/10.1016/j.jpowsour.2020.227992
Received 7 December 2019; Received in revised form 21 February 2020; Accepted 2 March 2020
Available online 9 March 2020
0378-7753/

interweaving structure endows the flexible rechargeable MABs, ZABs, and SCs with excellent electrochemical performance in terms of both activity and stability.

1. Introduction

The worldwide consciousness about environmental protection and sustainable energy production greatly accelerate the development of reliable electrochemical energy storage and conversion technologies [1,2], such as inflexible/flexible rechargeable metal-air batteries [3,4] (MeABs) and supercapacitors (SCs) [5–9]. Zinc-air batteries (ZABs) [10–14], magnesium-air batteries (MABs) [15,16] and SCs [17–20] have received widespread attention in large grid-scale energy storage and wearable electronic devices due to their low cost, high energy density, long shelf-life and environmental compatibility. However, the insufficient development of electrode materials remains a critical issue in achieving high energy/power density and long stability. Therefore, it is tremendously important to develop highly active multifunctional catalysts/electrode materials to catalyze the slow kinetic processes of oxygen reduction reaction (ORR)/oxygen evolution reaction (OER) for MeABs and increase the energy density of SCs [21–23].

Recently, manganese oxides (MnO_x) have demonstrated great potential in ZABs, MABs, and SCs due to their non-toxicity and good electrochemical properties [24–30]. Among all MnO_x materials, the MnO_2 has relatively higher catalytic activity [31]. Therefore, much effort has been devoted to synthesize MnO_2 with various morphologies and crystallographic structures, including nanowires (NWs) [32–34]. Actually, MnO_2 has several structural phases, such as α-MnO_2, β-MnO_2, γ-MnO_2, and λ-MnO_2, among which α-MnO_2 shows much higher discharge storage capacity than the other three when used as SC electrode material [35]. Furthermore, in terms of the morphology, the NWs of α-MnO_2 gave higher performance than the other three nanostructures, namely nanotubes, nanoparticles and nanorods [36]. For example, the MnO_2 NWs exhibited a higher capacitance (350 F g^{-1}) than that of MnO_2 nanorods (NRs) (243 F g^{-1}) [37]. Regarding the catalytic activity sequences of different phases of MnO_2, several orders have been observed, such as: $\alpha > \beta > \gamma$ [5,38], $\alpha > \beta > \delta$ [39], and $\alpha \sim \delta > \gamma > \lambda > \beta$ [40,41]. These results indicate that the electrochemical activity of MnO_2 catalysts strongly depend on their structures, e.g., size, crystalline phases and particle shape, etc. Unfortunately, the performance sequences and their corresponding theoretical analysis have not been totally understood in terms of the effects of crystal structures (α−, δ−, γ−, λ− and β−MnO_2) and morphology of MnO_2 for neither the ORR/OER catalytic activity/stability nor the capacitance of SCs [28,42,43]. Meanwhile, due to the intrinsic metastable forms of MnO_2 and low conductivity, some conductive additives needed to be added into the MnO_2 materials to increase the conductivity for application as electrode catalysts/materials [6,16,33,44,45]. Regarding the conductive additives, carbon nanotubes (CNTs), have better performance than other types of carbon materials, such as carbon black and graphenes, in terms of electrical conductivity and mass (i.e. oxygen) transfer [6,39,46]. CNTs can also be hybridized with MnO_2 to form catalysts or capacitive materials. Nevertheless, for a significant performance improvement, the morphology of the optimized material seems to be critically important [28,38–43]. Accordingly, multifunctional MnO_2-based materials, with suitable morphology to improve the performance of ORR/OER catalysts in MeABs, and capacitive electrode materials for SCs need to be developed. Apart from tuning the electrode catalysts/materials for the conventional SCs and batteries relying on liquid electrolyte for MeABs and SCs, their flexible devices, which are foldable, bendable, and potentially wearable, have recently attracted a great deal of attention. This is because the liquid electrolyte evaporates and leaks easily, resulting in safety issues when the material is environmentally hazardous. Therefore, the development of high performance, flexible and robust catalyst and capacitive materials that are suitable for the flexible configurations, seems to be even more important yet challenging.

In this work, we synthesized novel multifunctional composite materials, consisting of the intimately interweaved MnO_2 nanowires/nanorods and carbon nanotubes (henceforth referred to as MnO_2-NWRs/CNTs) with unique 3D electron conduction interpenetrating networks and high specific surface, using a facile two-step synthetic strategy, which included the solvothermal synthesis of MnO_2-NWRs interweaved with MnO_2-NWRs/CNTs, followed by their calcination. Comparative experimental investigation exhibited several beneficial characteristics of the hybrid, including that: (i) the unique 3D electron conduction interpenetrating networks provided an electron-transfer high way and formed the strong coupling and synergistic effect; (ii) high specific surface areas benefited the O_2 transport adsorption/desorption, exposure of more accessible active sites for both ORR and OER, and increase in capacity; (iii) the interweaved (110) crystal plane of MnO_2 can provide more oxygen vacancies, thus facilitating the rate-determining step of the ORR [33]; (iv) the MnO_2 (101) crystal plane can accelerate the migration of electron between MnO_2-NWRs and CNTs for OER; (v) the abundant reversible redox transitions in the MnO_2-NWRs/CNTs can promote the pseudocapacitive behavior of the materials; (vi) the flexible morphology also provides sufficient space for the electrocatalytic performance of flexible rechargeable devices. Due to these beneficial properties, the MnO_2-NWRs/CNTs catalysts have high electrochemical activity and power density in liquid and flexible ZABs and MABs. The liquid ZABs based on these catalyst materials exhibit conspicuous charge-discharge (C-D) stability (over 840 cycles), which is 2-fold that of Pt/C + IrO_2 based ZABs. The flexible MABs with the anion (Cl-/O-H-)-exchange membrane show the promising performance with high-power density of 82.9 mW cm^{-2} and valuable C-D stability. Moreover, the two-electrode SCs based on these materials exhibit superior capacitance and stability. Encouragingly, the interweaved and robust MnO_2-NWRs/CNTs materials appeared to improve the flexibility and stability of the flexible devices. These findings demonstrate that the MnO_2-NWRs/CNTs interweaving composites act as multifunctional materials and are promising candidate electrode materials for the next-generation of clean and reliable electrochemical energy storage/conversion devices, including the flexible ones.

2. Experimental section

2.1. Materials and catalyst synthesis

A one-step hydrothermal method was modified based on the redox reactions of $KMnO_4$ and $H_2C_2O_4$ (supplementary information) to synthesize MnO_2-NWRs. The interweaved MnO_2-NWRs/CNTs samples were synthesized using a further hydrothermal method. The schematic of the synthesis process and the sample formation is shown in Fig. 1a. In a typical synthesis, 1 g of the as-prepared MnO_2-NWRs powder and 0.05 g of CNTs were dispersed in 15 mL NH_4OH by stirring, and then transferred into an autoclave and heated at 150 °C for 5 h. The obtained precipitate was collected by centrifugation, washed with deionized water and ethanol, dried at 60 °C for 6 h, followed by calcination in a muffle furnace at 250 °C, 350 °C and 450 °C for 1 h, and the obtained samples were eventually designated as MnO_2-NRs/$CNTs_{250}$, MnO_2-NWRs/$CNTs_{350}$ and MnO_2-NWRs/$CNTs_{450}$. For comparison, the mixture of MnO_2 powder and CNTs (MnO_2+CNTs) was also prepared by directly mixing the MnO_2 powder with CNTs (weight ratio: 1:0.05) in ethanol, followed by drying in an oven at 60 °C for 1 h and calcination in a muffle furnace at 350 °C for 1 h (denoted as MnO_2+$CNTs_{350}$). Detailed procedures can be found in the supplementary information.

2.2. Characterization

The crystalline structure and morphology of the samples were analyzed by various techniques, including X-ray diffraction (XRD) analysis on a Philips PW3830 X-ray diffractometer (Philips Healthcare, Amsterdam, The Netherlands) using Cu Kα radiation (λ = 1.5406 Å); scanning electron microscopy (SEM) on a FEI Sirion 200 scanning electron microscope (FEI Company, Hillsboro, OR, USA), at 5 kV; X-ray photoelectron spectroscopy (XPS) on a Theta Probe electron spectrometer VG ESCALAB200i-XL, Thermo Scientific, Waltham, MA, USA; Transmission electron microscopy (TEM) and high resolution TEM (HRTEM) analysis on a JEOL 2010F transmission electron microscope (JEOL Ltd., Tokyo, Japan).

2.3. Measurements of electrochemical activity, battery and supercapacitor performance

The electrochemical tests were conducted using a three-electrode cell with 0.1 M KOH as electrolyte solution. The performance of the aqueous/flexible ZABs and MABs were evaluated using a galvanodynamic method and also the recurrent galvanic pulse method. The performance of the aqueous/flexible SCs was assessed using the recurrent galvanic pulse method. All battery measurements were performed under an air environment. Detailed procedures are provided in the supplementary information.

3. Results and discussion

3.1. Physical characterization

The XRD curves of the interweaved catalyst sample of MnO_2-NWRs/CNTs, synthesized through a mild hydrothermal process (Fig. 1a), followed by calcination in the furnace, are shown in Fig. 1b. The curves reveal that the diffraction peaks of MnO_2-NWRs/$CNTs_{350}$ agree well with those of the orthorhombic b-MnO_2 (JCPDS No. 24-0735, as denoted by sweat-heart) and CNTs (as denoted by rhombus), confirming the high purity of the sample. For further comparison, the MnO_2-NWRs samples, without addition of CNTs, were also synthesized by the one-step hydrothermal process at different temperatures and heat-treatment time, and calcined at 350 °C for 1 h. The obtained samples are designated as $MnO_{2(y\text{-}x)}$, where y and x represent the temperature and time of the hydrothermal treatment, respectively. The mixture of MnO_2 powder and CNTs was also prepared by directly mixing MnO_2 and CNTs, and calcination at 350 °C for 1 h (designated as MnO_2+$CNTs_{350}$). The data presented in Fig. S1 shows that $MnO_{2(y\text{-}x)}$, MnO_2+CNTs and MnO_2-NWRs/CNTs display different crystal parameters. Particularly, with the hydrothermal process for 4 h, the diffraction peaks of $MnO_{2(140\text{-}4)}$ (pure MnO_2) reveal a unique a-MnO_2 crystal structure (JCPDS NO. 44-0141) among all the $MnO_{2(y\text{-}x)}$ samples. The diffraction peaks of MnO_2+$CNTs_{350}$ corresponds well with those of the a-MnO_2 and CNTs. These observations verify that the crystal of MnO_2 can be transformed from a-to b-by the second step of the solvothermal tuning strategy (MnO_2-NWRs/$CNTs_{350}$ is b phase, and MnO_2+$CNTs_{350}$ is a phase). The SEM images displayed in Fig. 1c and Figs. S2–5, reveal the morphology evolution of the samples under different synthesis conditions. With different synthesis time (Fig. S2), the original morphology of $MnO_{2(140\text{-}x)}$

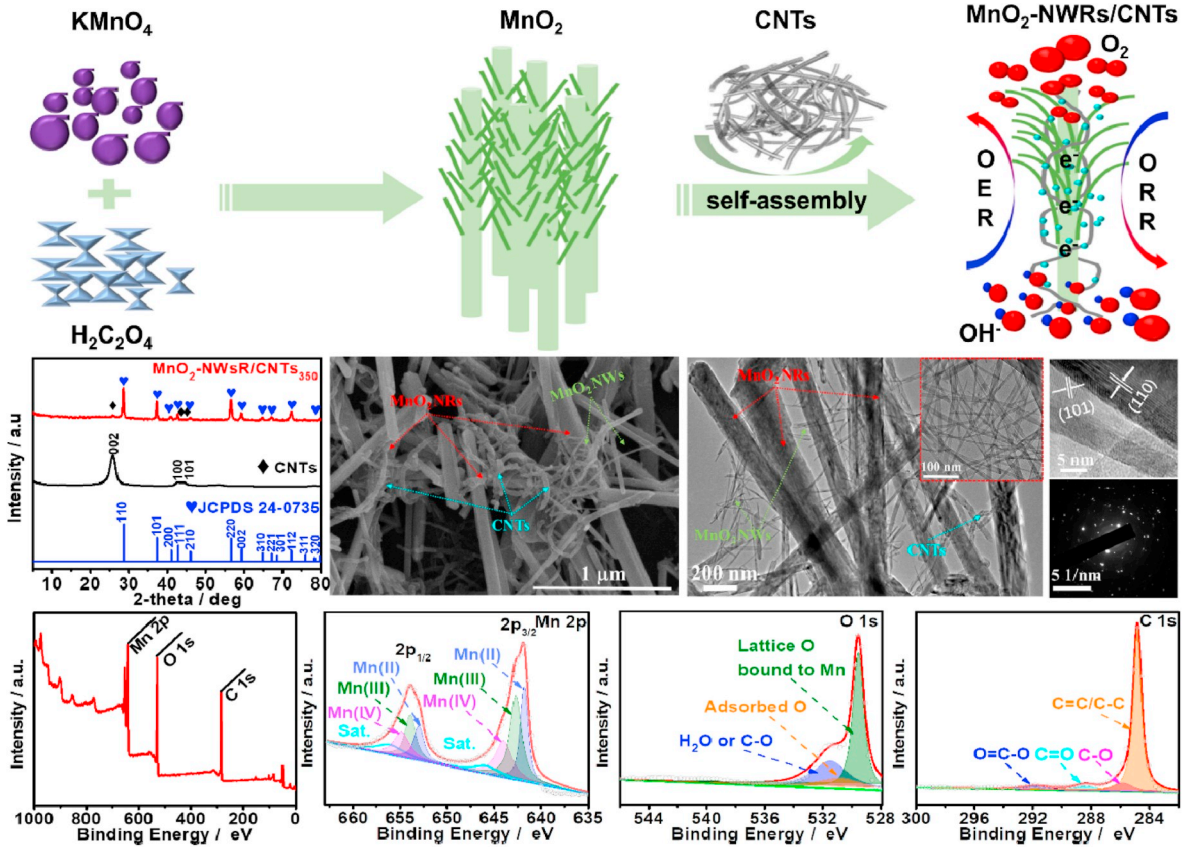

Fig. 1. (a) Scheme of the synthesis of MnO_2-NWRs/CNTs; (b) XRD patterns of MnO_2-NWRs/$CNTs_{350}$ catalyst and CNTs; (c) SEM image of MnO_2-NWRs/$CNTs_{350}$; (d) TEM image of MnO_2-NWRs/$CNTs_{350}$ (inset: TEM image of the red dashed box); (e) HRTEM image of MnO_2-NWRs/$CNTs_{350}$; (f) SAED pattern of MnO_2-NWRs/$CNTs_{350}$; (g) XPS survey spectrum of MnO_2-NWRs/$CNTs_{350}$; (h–j) Mn 2p, O 1s and C 1s XPS spectra, respectively. (For interpretation of the references to colour in this figure legend, the reader is referred to the Web version of this article.)

(uneven NRs) turns into a homogeneous mixture of NWs and NRs (NWs produced by NRs, Fig. S5), then further changes to a cube shape, and eventually transforms into short NRs. The morphology evolution of $MnO_{2(y-4)}$ also follows a similar rule (uneven NRs turn into a cube shape and short NRs) at different synthesis temperatures (Fig. S3). Typically, the flexible MnO_2-NWRs/$CNTs_{350}$ sample forms a unique 3D electron conduction interpenetrating networks by intimately interweaving CNTs and MnO_2-NWRs, which is very different from the MnO_2-NRs/$CNTs_{250}$ (without NWs and interpenetrating networks), the MnO_2-NWRs/$CNTs_{450}$ (with a broken electron conduction interpenetrating networks) and the MnO_2+$CNTs_{350}$ (without flexible NWs and electron conduction interpenetrating networks), indicating a combined physical and chemical interaction between MnO_2 and CNTs (Fig. S4). The TEM images indicate that a large number of MnO_2 NWs grow on the surface of the MnO_2-NRs and evenly mix with CNTs (Fig. 1d). The MnO_2NWRs/$CNTs_{350}$ sample is more flexible and robust than the pure MnO_2 (Figs. S5a–b), which is favorable for the flexible devices [11,47]. Also, the XRD pattern and the high-resolution TEM (HRTEM) image of the MnO_2NWRs/$CNTs_{350}$ sample reveal that it exhibits monocrystalline characteristics, corresponding to the selected area electron diffraction (SAED) pattern (Figs. S5c–d). Pure MnO_2 does not show multiple diffraction spots, indicating that pure MnO_2 grows along the [110] direction [42]. However, the HRTEM image of MnO_2-NWRs/$CNTs_{350}$ shown in Fig. 1e reveal that it is the [110] and [101] view of MnO_2-NWRs. The SAED pattern in Fig. 1f reveals a polycrystalline feature with indexed diffraction rings, which is in agreement with the XRD pattern of MnO_2 (Fig. 1b). The MnO_2-NWRs/$CNTs_{350}$ displays the multiple diffraction spots, implying that the primary MnO_2-NWRs are precisely oriented with respect to each other and grow separately along the [110] and [101] directions (Fig. 1b, e and f) [28,42]. The [110] and [101] crystal planes clearly extend throughout the entire catalyst, probably favouring the performance of both ORR and OER [33,48–50]. The Brunauer, Emmett and Teller (BET) specific surface areas of MnO_2-NWRs/$CNTs_{350}$ is 285.7 m^2 g^{-1}, which is larger than that of the $MnO_{2(y-x)}$, pure MnO_2 and MnO_2+CNTs catalysts (Table S1 and Fig. S6). High specific surface areas benefit the O_2 transport adsorption/desorption, exposure of more accessible active sites for both ORR and OER, and increase in capacity [47]. It also provides sufficient space for the electrocatalytic performance of flexible rechargeable battery devices.

To further confirm the chemical composition and state of the samples, the XPS spectra of C, O, and Mn peak regions were recorded, as shown in Fig. 1g. There are no evident peaks associated with contamination, which is in a good agreement with the results obtained by XRD analysis (Fig. 1b). For Mn *2p*, two core-level signals of Mn *2p* located at ~642.2 and 653 eV are attributed to Mn $2p_{3/2}$ and Mn $2p_{1/2}$, respectively (Fig. 1h). The Mn $2p_{3/2}$ spectra display four peaks with binding energies of 640.8, 642.6, 643.5, and 645.8 eV, which can be assigned to Mn (II), Mn (III), Mn (IV), and the satellite, respectively. The weakest satellite peak originates from the charge transfer from the outer electron shell to an unoccupied orbit with higher energy [51,52]. The O *1s* spectrum in Fig. 1i exhibits three features, corresponding to the C–O/H_2O (531.9 eV), O^-/O_2^{2-} (531.3 eV) and lattice oxygen bonding with Mn (Olatt) (529.6 eV) [52,53]. In addition, the XPS spectrum of C *1s* is divided into the O═C–O band (291.8eV), C═O band (288.4eV), C–O band (285.8 eV) and C═C/C–C band (284.8eV) (Fig. 1j). The C–O bond and Mn–OH bond are easy to etherify, thereby facilitating the transformation of the C–O–Mn band, which reasonably rendered the composite material more robust. Moreover, the MnO_2-NWRs/$CNTs_{350}$ sample has low binding energy, confirming the migration of the electron cloud. It is worth noting that the XPS results suggest the existence of Mn^{II}/Mn^{III} and Mn^{III}/Mn^{IV} species, which are regarded as active sites for both OER/ORR and pseudocapacitance [7,33,48,49].

3.2. Electrochemical measurements

To better evaluate the ORR and OER activity of the $MnO_{2(y,x)}$, MnO_2-NRs/$CNTs_{250}$, MnO_2-NWRs/$CNTs_{350}$, MnO_2-NWRs/$CNTs_{450}$ and MnO_2+$CNTs_{350}$ samples, the IrO_2 and Pt/C catalysts were chosen as the reference baselines. As shown in Fig. 2a and b and Fig. S7, the ORR curve of the MnO_2-NWRs/$CNTs_{350}$ catalyst exhibits a much lower overpotential (at a current density of 3 mA cm^{-2}) compared to those of the IrO_2, $MnO_{2(y,x)}$, MnO_2-NRs/$CNTs_{250}$, MnO_2-NWRs/$CNTs_{450}$ and MnO_2+$CNTs_{350}$ catalysts, while Pt/C exhibits a more positive overpotential. Meanwhile, the OER curve of the MnO_2-NWRs/$CNTs_{350}$ catalyst exhibits a much lower overpotential (at a current density of 10 mA cm^{-2}) among all the tested samples, while IrO_2 exhibits a more positive overpotential. Based on the results of the above structural analysis, the MnO_2-NWRs grows along the (110) and (101) crystal plane directions. It is well-known that the (110) crystal plane of MnO_2 creates more oxygen vacancies to improve the ORR catalytic process [28,29,39,40], and the (101) crystal plane improves the reactant-insertion to accelerate the OER process [34,41]. Thus, as expected, the MnO_2-NWRs/$CNTs_{350}$ exhibits the highest activity toward both ORR and OER among the tested samples, which is related to the crystal orientation of MnO_2-NWRs in the catalyst as well as the largest effective catalytic surface area. This catalytic surface area is obtained by measuring the electrochemically active surface area (ECSA) and calculating it from the electrochemical double layer capacitance (C_{dl}) (Table S1). The data displayed in Table S1 reveals that the MnO_2-NWRs/$CNTs_{350}$ has a larger ECSA of 18.20 mF cm^{-2} than those of $MnO_{2(y-x)}$ (1.67–1.80 mF cm^{-2}), pure MnO_2 (4.51 mF cm^{-2}), MnO_2-NRs/$CNTs_{250}$ (8.21 mF cm^{-2}), MnO_2-NWRs/$CNTs_{450}$ (8.72 mF cm^{-2}) and MnO_2+$CNTs_{350}$ (9.81 mF cm^{-2}). The rotating-disk electrode with different rotational speeds was applied to reveal the ORR kinetics of this MnO_2-NWRs/$CNTs_{350}$ catalyst (Figs. S8–10). The results indicate that the MnO_2/$CNTs_{350}$ catalyst has a larger electron-transfer number (n, 3.89) than those of $MnO_{2(y-x)}$ (2.87–3.38), pure MnO_2 (3.67), MnO_2-NRs/$CNTs_{250}$ (3.73), MnO_2-NWRs/$CNTs_{450}$ (3.85) and MnO_2+$CNTs_{350}$ (3.81). Additionally, the value is comparable to that of the Pt/C catalyst (3.98), suggesting that the MnO_2-NWRs/$CNTs_{350}$ catalyst favors a four electron ORR pathway (Fig. 2d and Figs. S11d–f). The Tafel slope of MnO_2-NWRs/$CNTs_{350}$ is ~69 mV dec^{-1}, which is much smaller than its counterparts obtained with other synthesis conditions and even lower than that of the IrO_2 catalyst (71.3 mV dec^{-1}), indicating the improved OER kinetics of MnO_2-NWRs/$CNTs_{350}$ (Fig. 2d and Figs. S11d–f). The turnover frequency (TOF, which is used to further understand the intrinsic OER activity) of MnO_2-NWRs/$CNTs_{350}$ is ~1.2 × 10^{-3} s^{-1} at an OER overpotential of 350 mV, revealing that the metal atom sites contribute to the activities [53]. Notably, the TOF value of MnO_2-NWRs/$CNTs_{350}$ is greatly increased to ~3 × 10^{-2} s^{-1} at an OER overpotential of 600 mV, suggesting that the electron transfer rate on the active sites increases rapidly as the overpotential increases. In general, the difference (ΔE) between the ORR potential at 3 mA cm^{-2} and the OER potential at 10 mA cm^{-2} metrics is responsible for the overall oxygen electrode activity (Fig. 2e) [40]. The smaller the ΔE is, the closer to a fast oxygen reaction kinetics the electrode activity is. By this metric, the MnO_2-NWRs/$CNTs_{350}$ reaches to the ΔE of 0.98 V, which is much smaller than those with the precious metal catalysts, including Pt/C (1.20V), IrO_2 (1.49V) and the $MnO_{2(y-x)}$ catalysts (Table S1). In addition, the result of the analysis by electrochemical impedance spectroscopy (EIS) shown in Fig. S12 indicates that the MnO_2-NWRs/$CNTs_{350}$ catalyst has the lowest resistance (R_s, 5.6 Ω) among all tested catalyst samples ($MnO_{2(y-x)}$: 48.2–82.3 Ω, pure MnO_2: 40.5 Ω, MnO_2-NRs/$CNTs_{250}$: 25.3 Ω, MnO_2-NWRs/$CNTs_{450}$: 29.8 Ω and MnO_2+$CNTs_{350}$: 20.6 Ω). According to the ECSA obtained by capacitance measurements, the pure MnO_2 catalyst realizes a lower resistance (40.5 Ω) and larger ECSA (4.51 mF cm^{-2}) than other $MnO_{2(y-x)}$ catalysts (48.2–82.3 Ω and 1.67–1.80 mF cm^{-2}). Concretely, as the morphology of MnO_2 is transformed from NRs (such as $MnO_{2\ (140-2)}$ and $MnO_{2\ (120-4)}$) to the coexistent NRs and NWs (such as pure MnO_2), the R_s values and ECSA alternate accordingly ($MnO_{2\ (140-2)}$: 50.7 Ω and 1.72 mF cm^{-2}, $MnO_{2\ (120-4)}$: 49.2 Ω and 1.69 mF cm^{-2}, and pure MnO_2: 40.5 Ω and 4.51 mF cm^{-2},

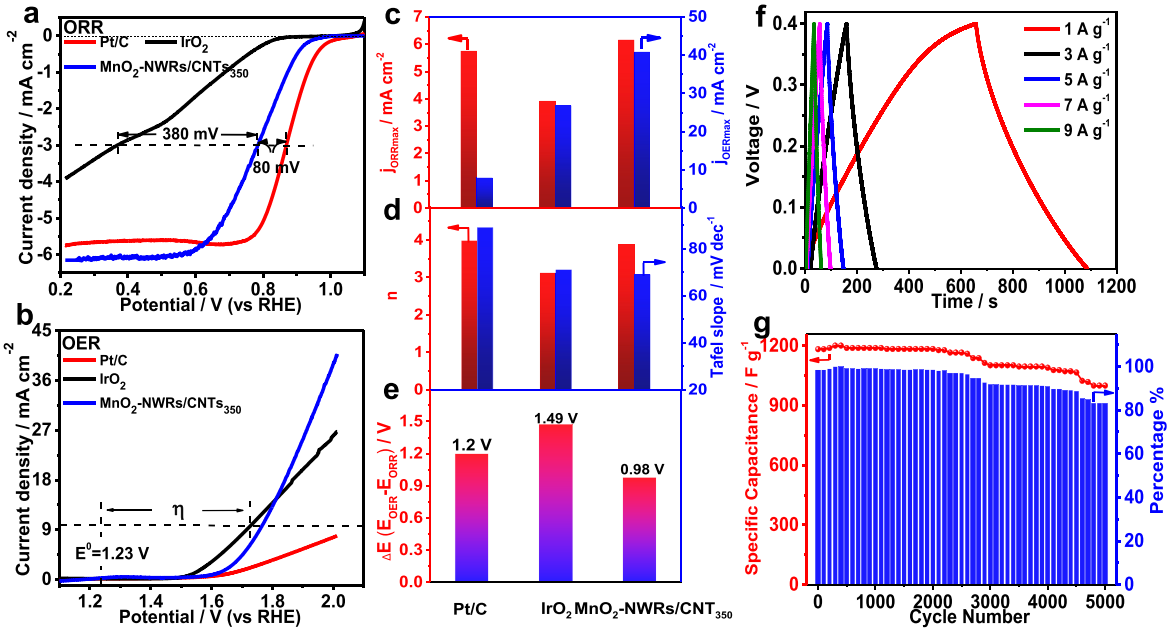

Fig. 2. (a and b) ORR and OER polarization curves for Pt/C, IrO_2 and MnO_2-NWRs/$CNTs_{350}$ catalysts; (c) The max current density of ORR and OER; and (d) the number of electron transfer and the Tafel slope of Pt/C, IrO_2 and MnO_2-NWRs/$CNTs_{350}$ catalysts; (e) The △E of Pt/C, IrO_2 and MnO_2-NWRs/$CNTs_{350}$ catalysts; (f) Galvanostatic charge/discharge curves of MnO_2-NWRs/$CNTs_{350}$ at different current densities in three-electrode system; (g) Cycle performance of the 5000 cycle life test at a galvanostatic charge-discharge current density of 9 A g^{-1}.

respectively). The results suggest that the coexistence of NRs and NWs is in favor of electrocatalysis behavior. Meanwhile, the MnO_2-NWRs/$CNTs_{350}$ catalyst manifests a lower resistance (R_s: 5.6 Ω) and larger ECSA (18.20 mF cm^{-2}) than the pure MnO_2 (R_s: 40.5 Ω and ECSA: 4.51 mF cm^{-2}), induced by the formation of 3-dimensional (3-D) electron conduction interpenetrating networks through a strong coupling between MnO_2-NWRs and CNTs. Hence, the strong coupling/synergistic effects between MnO_2-NWRs and CNTs, the unique 3-D electron conduction interpenetrating networks and the coexistence of the (110) and (101) crystal plane together enhance the ORR and OER activity by accelerating the rate-determining step of ORR ($(MnOOH)_2\cdots O_{2ads} + e^- = MnOOH\bullet\bullet\bullet O_{ads} + OH^- + MnO_2$) and OER ($MnOOH\bullet\bullet\bullet O_{ads} + OH^- + MnO_2 + e^- = (MnOOH)_2\cdots O_{2ads}$ and the desorption of O_2) [33,54].

To obtain the optimum working window of MnO_2-NWRs/$CNTs_{350}$, cyclic voltammetry (CV) studies are first conducted with different potential scan rates of 0–0.3, 0–0.4 and 0–0.5 V at 100 mV s^{-1} (Fig. S13a). The MnO_2-NWRs/$CNTs_{350}$ electrode displays a stable work potential window in the voltage range from 0 to 0.4 V. The CV studies were also carried out at scan rates of 10–1000 mV s^{-1} under a stable work potential window. As shown in Fig. 2b, in Fig. S13b, the potential window remains stable at different scan rates in the range from 10 to 1000 mV s^{-1}. The data shown in Fig. 2f illustrates the galvanostatic charge-discharge (C-D) curves of MnO_2-NWRs/$CNTs_{350}$ under the potential range from 0 to 0.4 V at different current densities in the range from 1 to 9 A g^{-1}. The specific capacitance is 1183 F g^{-1} at 1 A g^{-1}, which is superior to that of the other MnO_x-based materials (Table S1). The high specific capacitance indicates that the 3-D electron conduction interpenetrating networks and the coexistence of NRs and NWs can promote the pseudocapacitance of the material. In addition, the charge/discharge cycles at a current density of 1 A g^{-1} over 5000 cycles were run to evaluate the stability of the MnO_2/$CNTs_{350}$ nanocomposites (Fig. 2g). The MnO_2-NWRs/$CNTs_{350}$ electrode achieves a high specific capacitance of 1000–1202 F g^{-1}, and maintains a stable coulombic efficiency of 83% for up to 5000 cycles. The change of electronic structure and phase conversion of the material leads to the slight attenuation of the specific capacitance, which is proved by the breakdown of the 3-D electron conduction interpenetrating networks (Fig. S14a). In contrast, taking advantage of the lack of changes in the phase conversion and the robustness of the 3-D electron conduction interpenetrating networks, the MnO_2-NWRs/$CNTs_{350}$ exhibits a stable coulombic efficiency reaching to 98% after 2200 cycles (Fig. S14b). Therefore, the 3-D electron conduction interpenetrating networks and flexible NWs can greatly improve the pseudocapacitance of the MnO_2-NWRs/$CNTs_{350}$ composites with high BET specific surface areas and ECSA. It is believed that the reversible redox transitions of Mn^{III}/Mn^{IV} species, as well as the exchange of cations and/or protons with the electrolyte must be responsible for the high performance of the material. Moreover, it is worth noting that the MnO_2-NWRs/$CNTs_{350}$ (b-) as a multifunctional catalyst material can show more active electrocatalytic behaviour than MnO_2+$CNTs_{350}$ (a-), which is different from the above-mentioned general rule (activity: a- > b-). The notable phenomenon arises from the formation of the unique 3-D electron conduction interpenetrating networks structure and the strong coupling/synergistic effects between MnO_2-NWRs and CNTs. The above results directly demonstrate that the electrochemical activity of the MnO_2 based materials depends on both the crystal structure and morphology.

3.3. Electrochemical energy devices performances

The excellent performance of the ORR, OER and pseudocapacitance suggests that the MnO_2-NWRs/$CNTs_{350}$ composite material is an ideal electrode material for MeABs and SCs (Fig. S15). To determine the practicability of MnO_2-NWRs/$CNTs_{350}$, the aqueous ZABs, MABs and SCs were constructed. The power density curves and discharge polarization curves of MABs with the Pt/C and MnO_2-NWRs/$CNTs_{350}$ cathodes, are displayed in Fig. 3a. The current density of the MnO_2-NWRs/$CNTs_{350}$ cathode reaches to 500 mA cm^{-2} at 1.0 V, which is 2-fold that of Pt/C (250 mA cm^{-2} at 1.0 V). The MnO_2-NWRs/$CNTs_{350}$ demonstrates superior power density with a maximum value of 640 mW cm^{-2}, and outperforms the Pt/C cathode (350 mW cm^{-2}), as well as the reported MnO_2/CNTs-OH (79.2 mW cm^{-2}) and MnO_2/C (62.4 mW cm^{-2}) cathodes [16]. Importantly, the MABs with MnO_2-NWRs/$CNTs_{350}$ exhibits remarkable operational stability. The discharge curve of the

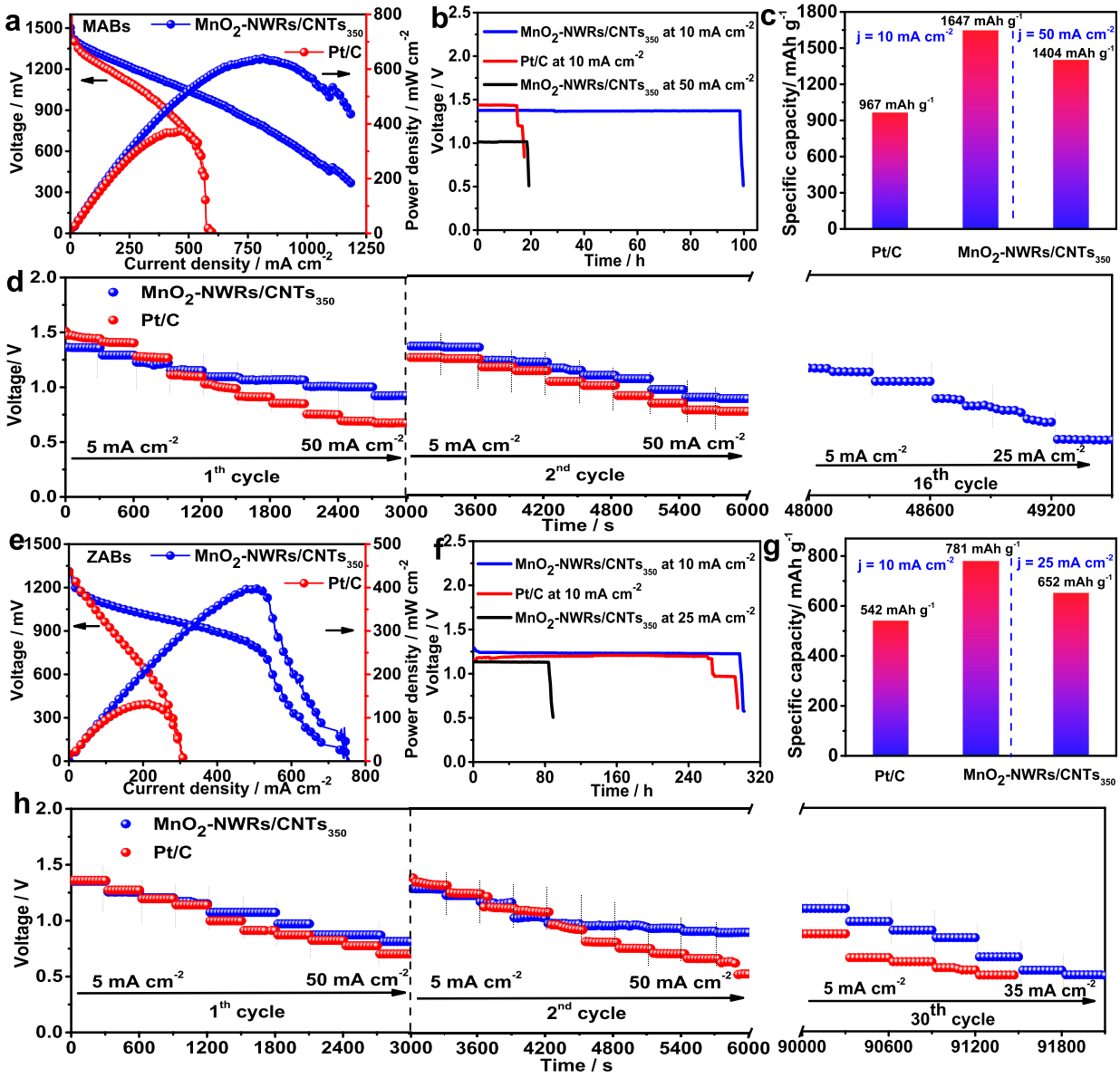

Fig. 3. (a) Polarization curves and corresponding power density plots of the MABs using MnO_2-NWRs/$CNTs_{350}$ and Pt/C as the air cathode catalysts; (b) Typical discharge curves of MABs at different current densities; (c) Corresponding specific capacity of MABs; (d) the cycles of discharge curve at the current densities range of 5–50 mA cm^{-2}/5 min per current density; (e) Polarization curves and corresponding power density plots of the ZABs using MnO_2-NWRs/$CNTs_{350}$ and Pt/C as the air cathode catalysts; (f) Typical discharge curves of ZABs at different current densities; (g) Corresponding specific capacity of ZABs; (h) The cycles of the discharge curve at the current densities range of 5–50 mA cm^{-2}/5 min per current density.

MnO_2-NWRs/$CNTs_{350}$ cathode lasts over 96 h with almost no voltage drop at a constant current of 10 mA cm^{-2} (Fig. 3b), demonstrating an excellent stability relative to the Pt/C cathode which lasts only 18 h. The discharge voltage of MABs remains unchanged over 20 h even at 50 mA cm^{-2}. Additionally, the specific capacitance of the MnO_2-NWRs/$CNTs_{350}$ cathode reaches to 1647 mA h g^{-1} at 10 mA cm^{-2} and 1404 mA h g^{-1} at 50 mA cm^{-1} (normalized to the weight of the consumed magnesium) (Fig. 3c). Evidently, the MnO_2-NWRs/$CNTs_{350}$ cathode exhibits the highest power density and specific capacity among those of the $MnO_{2(y-x)}$, MnO_2-NRs/$CNTs_{250}$, MnO_2-NWRs/$CNTs_{450}$ and MnO_2+$CNTs_{350}$ cathodes, which is consistent with the ORR activity of these catalysts (Figs. S7a–c and Figs. S16a–c). It is noteworthy that such high-power density and specific capacity of the MnO_2-NWRs/$CNTs_{350}$ cathode are first reported throughout the literature. The MnO_2-NWRs/$CNTs_{350}$ electrode also exhibits greater stability than the Pt/C cathode in the galvanostatic discharge (GD) cycles with different current densities in the range from 5 to 50 mA cm^{-2} (Fig. 3d). This is further proved by the finding that the corresponding GD cycles of the MnO_2-NWRs/$CNTs_{350}$ cathode still remains operational beyond the 16th cycle in the range from 5 to 25 mA cm^{-2}, whereas the Pt/C cathode breaks down after only its 8th cycle.

In addition, the home-made cathodes were also used for the ZABs. The results presented in Fig. 3e and Figs. S16d–f reveal that the MnO_2-NWRs/$CNTs_{350}$ cathode affords the maximum peak power density of 400 mW cm^{-2}, which is notably higher than that of the Pt/C cathode (120 mW cm^{-2}) and those of the home-made cathodes. The working voltages are stabilized at ~1.26 V when operated at 10 mA cm^{-2} for 300 h with almost no noticeable drop, displaying high discharge performance (Fig. 3f). The MnO_2-NWRs/$CNTs_{350}$ possesses the corresponding specific capacity of 781 mAh g^{-1} at 10 mA cm^{-2} and 652 mAh g^{-1} at 25 mA cm^{-2} (Fig. 3g), which are clearly higher than those of the Pt/C (542 mA h g^{-1} at 10 mA cm^{-2}) and $MnO_{2(y-x)}$, MnO_2-NRs/$CNTs_{250}$, MnO_2-

NWRs/CNTs$_{450}$ and MnO$_2$+CNTs$_{350}$ cathodes (Figs. S16d–f). Additionally, the MnO$_2$-NWRs/CNTs$_{350}$ cathode gives excellent discharge performance (such as stability and repeatability) compared with the Pt/C cathode under the GD cycles at the different current densities in the range from 5 to 50 mA cm^{-2} (Fig. 3h). All the above results indicate that the MnO$_2$-NWRs/CNTs$_{350}$ is a highly active and stable oxygen catalyst for both OER and ORR, which can be widely used in primary MABs and ZABs.

The high performance of the MnO$_2$-NWRs/CNTs$_{350}$ cathode was not only evaluated in primary MABs and ZABs, but also tested in rechargeable electronic devices. The MnO$_2$-NWRs/CNTs$_{350}$ cathode exhibits higher discharge voltage and considerably lower charge voltage than those of the Pt/C + IrO$_2$ air cathode at different current densities in a wide range from 5 to 100 mA cm^{-2} (Fig. 4a). As shown in Fig. 4b, the MnO$_2$-NWRs/CNTs$_{350}$ cathode displays remarkable cycling stability with a negligible voltage change (only 0.08 V after 140 h), better than that of the Pt/C + IrO$_2$ air cathode under a typical C-D cycling curve at 5 mA cm^{-2}. The C-D overpotential of the MnO$_2$-NWRs/CNTs$_{350}$ cathode is evidently smaller than that of the Pt/C + IrO$_2$ cathode in the current density range from 0 to 100 mA cm^{-2}. Notably, the C-D overpotential of the MnO$_2$-NWRs/CNTs$_{350}$ cathode is only 0.1 V at 5 mA cm^{-2} (Fig. 4c). At a high current density of 100 mA cm^{-2}, the MnO$_2$-NWRs/CNTs$_{350}$ cathode still shows a lower overpotential (0.98 V) than those of the Pt/C + IrO$_2$ (1.68 V), MnO$_{2(y-x)}$, MnO$_2$/CNTs$_{250}$, MnO$_2$/CNTs$_{450}$ and MnO$_2$+CNTs$_{350}$ cathodes (Figs. S16g–i). The C-D cycling for over 100 h at 25 mA cm^{-2} further demonstrates the stability of the ZABs (Fig. 4d). These results clearly reveal that the MnO$_2$-NWRs/CNTs$_{350}$ catalyst is a highly competitive alternative to the commercial Pt/C + IrO$_2$ catalyst for practical application in the rechargeable ZABs. Furthermore, the C-D cycling measurement of aqueous-SC suggests a superior capacitance of 246 F g^{-1} at 20 A g^{-1} (Fig. 4e). Therefore, the newly developed multifunctional catalyst further exhibits great potential for the aqueous-rechargeable ZABs and aqueous-SCs due to its excellent ORR, OER and pseudocapacitance performance.

Besides the unique 3-D electron conduction interpenetrating networks with multifunctional properties, the NWs/NRs in MnO$_2$-NWRs/CNTs$_{350}$ make the hetero-material more flexible and robust, further enhancing the possibility of its application on flexible devices. As a proof-concept application, the flexible rechargeable ZABs, MABs and SCs were constructed in this study. For flexible MABs, notably, the anion (Cl^-)-exchange membranes not only can provide the flexibility of flexible MABs, but also can inhibit the hydrogen evolution reaction and the migration of Mg^{2+}. Thus, it will further enhance the performance of flexible MABs. As anticipated, the flexible MABs possess an open-circuit voltage (OCV) as high as 1.32 V and a high-power density of 82.9 mW cm^{-2} (Fig. 5a). The GD measurements exhibit a long-term stability without noticeable voltage degradation at different current density. Moreover, the MABs display a stable discharge voltage of 1.35 V over 25 h at 2 mA cm^{-2} (Fig. 5b), and have an incredible C-D cycling stability (over 4 h) and a low C-D voltage gap of 1.02 V at 5 mA cm^{-2}, which have never been previously reported in literature (Fig. 5c). For flexible ZABs, the anion (OH^-)-exchange membrane can prevent the migration of Zn^{2+} by separating the cathode and the anode and the production of K_2CO_3 ($2KOH + CO_2 = K_2CO_3 + H_2O$)/$KHCO_3$ ($KOH + CO_2 = KHCO_3$) by the ion-exchange reaction, thereby further enhancing the activity and stability [10,55]. As shown in Fig. 5d, the flexible ZABs exhibit an OCV of 1.31 V, and the maximal power density reaches to 43 mW cm^{-2} at 68 mA cm^{-2}. The working voltage plateau reaches 1.02–1.30 V at a current density range from 2 to 10 mA cm^{-2}, corresponding to the working time of 13–40 h (Fig. 5e). In particular, the ZAB exhibits a negligible performance degradation over 40 h at a constant current density of 2 mA cm^{-2}. The data shown in Fig. 5f reveals that the initial voltage gap is only ~0.76 V under the typical C-D cycle at 5 mA cm^{-2}. The C-D voltage plateau and voltage gap (0.78 V) are maintained very well after continuous C-D cycling for more than 20 h. Therefore, armed with high activity and stability, the MnO$_2$-NWRs/CNTs$_{350}$ catalyst could offer the promising performance of flexible MeABs as it better prevented the side reaction due to the anion (Cl^-/OH^-)-exchange membrane. For flexible SCs, the CV curve demonstrates a typical SC behavior in the range from 0 to 0.8 V at 100 mV s^{-1} (Fig. 5g). Moreover, the shapes of all CV curves

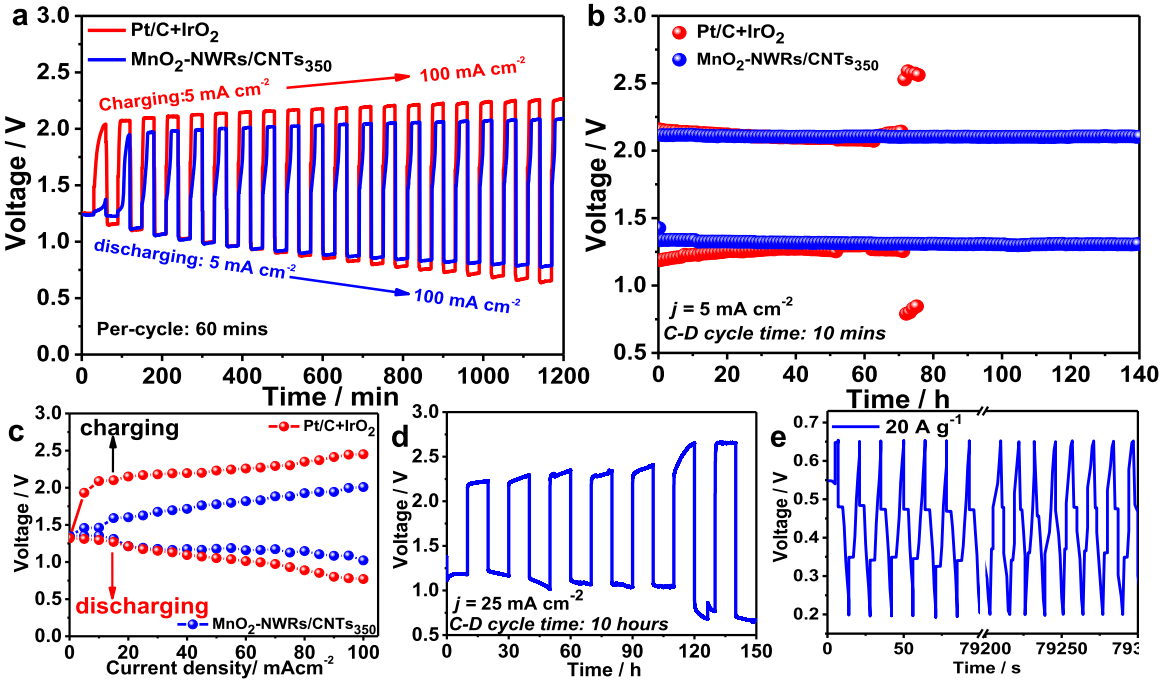

Fig. 4. (a) C-D cycles at the current density range of 5–100 mA cm^{-2}/60 min per current density with Pt/C + IrO$_2$ and MnO$_2$-NWRs/CNTs$_{350}$ as the air cathode catalysts; (b) Cycling data at 5 mA cm^{-2} in 10 min per cycle using Pt/C + IrO$_2$ and MnO$_2$-NWRs/CNTs$_{350}$ as the air cathode catalysts; (c) Charge and discharge polarization (V-i) curves of the rechargeable ZABs using Pt/C + IrO$_2$ and MnO$_2$-NWRs/CNTs$_{350}$ as the air cathode catalysts; (d) Cycling data at 25 mA cm^{-2} in 10 h per cycle using the MnO$_2$-NWRs/CNTs$_{350}$ catalyst as the air cathode catalysts; (e) The C-D cycles of two electrode SCs in 0.1 M KOH.

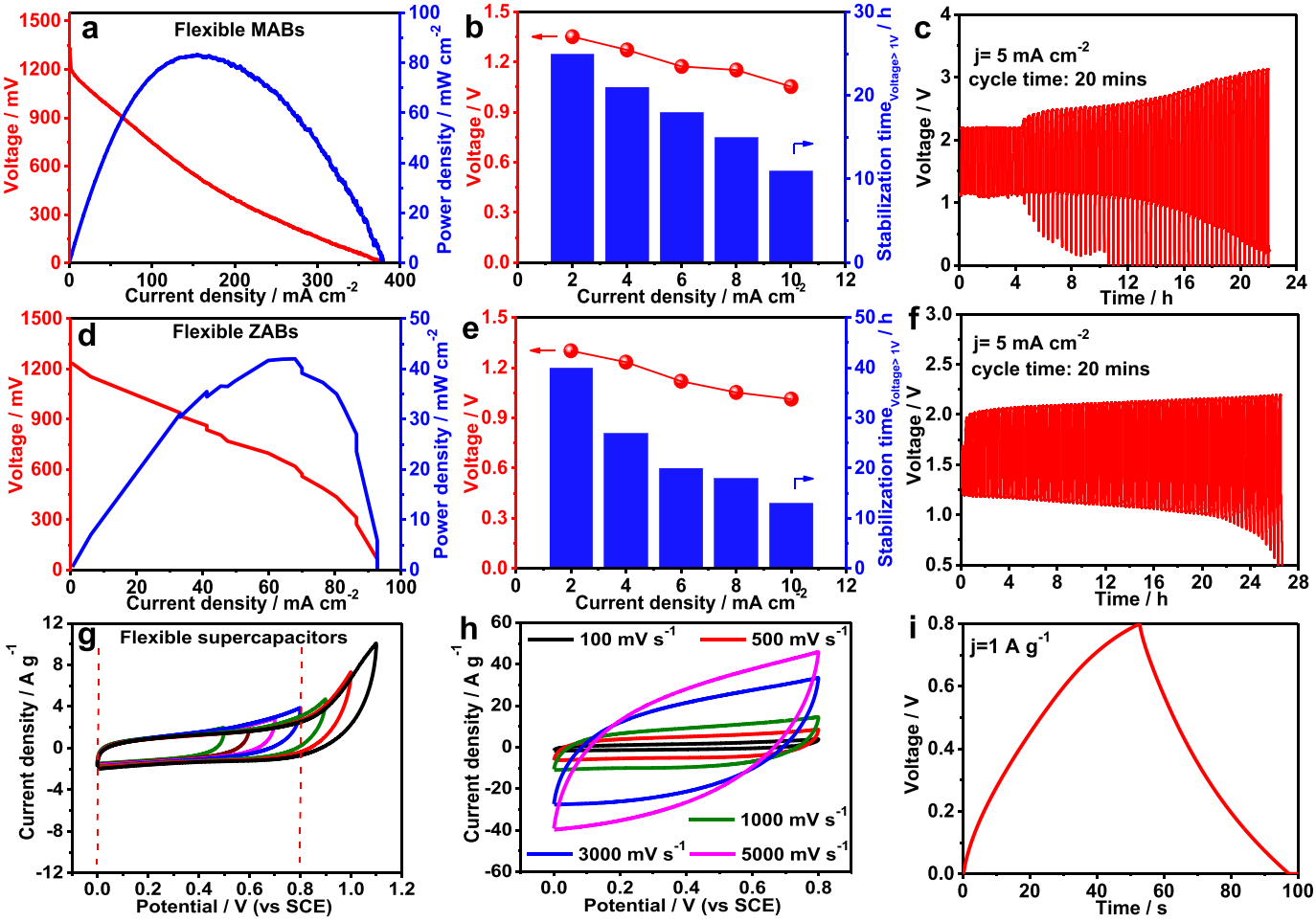

Fig. 5. Flexible MABs using MnO_2-NWRs/$CNTs_{350}$ as the air cathode catalyst. (a) Polarization curves and corresponding power density plots; (b) The OCV and stabilization time at the current densities range of 5–50 mA cm^{-2}; (c) Cycling data at 5 mA cm^{-2} in 20 min per cycle. The flexible ZABs using MnO_2-NWRs/$CNTs_{350}$ as the air cathode catalysts. (d) Polarization curves and corresponding power density plots; (e) The OCV and stabilization time at the current densities range of 5–50 mA cm^{-2}; (f) Cycling data at 5 mA cm^{-2} in 20 min per cycle. The flexible SCs using MnO_2-NWRs/$CNTs_{350}$ as the air cathode catalysts. (g) CV curves at different voltage windows; (h) CV curves at different scan rates of 100–5000 mV s^{-1}; (i) the charge-discharge process at 1 A g^{-1}.

are nearly symmetrical at different scan rates (even at 1000 mV s^{-1}), revealing a perfect SC behavior (Fig. 5h). The flexible SC represents a good symmetrical capacitive characteristic (70 F g^{-1}) by the C-D test at a current density of 1 A g^{-1}, and accompanies the pimping resistance (R_s: 3.2 Ω) (Fig. 5i and Fig. S17). The results indicate that the robust and flexible MnO_2-NWRs/$CNTs_{350}$ catalyst can promote the flexibility and reduces the contact resistance of flexible SCs, achieving high performance. Thus, the flexible and high-activity MnO_2-NWRs/$CNTs_{350}$ is also a feasible candidate for the electrode material of wearable energy conversion devices.

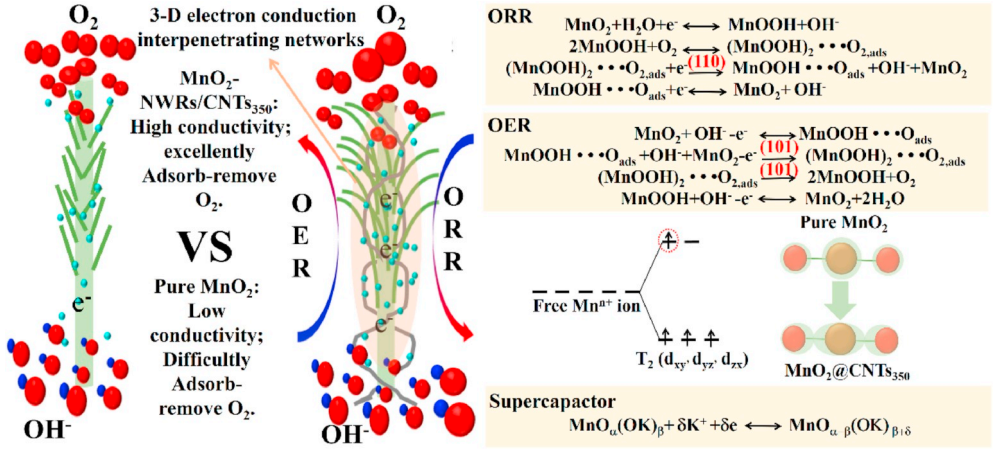

Fig. 6. Schematic of the electrochemical mechanism of the ORR, OER and supercapacitors processes with MnO_2-NWRs/$CNTs_{350}$ as the cathode catalyst/material.

The multifunctional MnO_2-NWRs/$CNTs_{350}$ catalyst material displays better ORR, OER and capacitance performance than those of IrO_2, Pt/C, $MnO_{2(y-x)}$, MnO_2-NRs/$CNTs_{250}$, MnO_2-NWRs/$CNTs_{450}$, MnO_2+$CNTs_{350}$ and the widely reported MnO_x based materials (Table S1). To further explain the improved ORR/OER kinetics and high specific capacitance of MnO_2-NWRs/$CNTs_{350}$, the 3-D electron conduction interpenetrating networks and their associated electrochemical mechanism are also examined in this paper. As shown in Fig. 6, the ORR on MnO_2-NWRs/$CNTs_{350}$ follows first-order kinetics toward the O_2 concentration and obeys the 4-electron process [55]. The unique 3-D structure of electron conduction interpenetrating networks rapidly reduces the OH^- concentration in nearby spaces and creates buffer zones, providing a thermodynamically favorable environment for the detachment of OH^-. Many Mn^{II}/Mn^{III} and Mn^{III}/Mn^{IV} species that act as oxygen acceptor/donor can assist the charge transfer to molecular (and adsorbed) oxygen, thus accelerating the ORR process. Furthermore, the MnO_2-NWRs/$CNTs_{350}$ catalyst grows along the (110) direction; the (110) crystal plane of MnO_2 can facilitates the rate-determining step by providing more oxygen vacancies [42,55,56]. For the OER process, on the other hand, the rate-determining step is significantly influenced by the insertion of a reactant [57]. The (101) crystal plane of the MnO_2-NWRs/$CNTs_{350}$ can ameliorate the reactant-insertion for electrochemical performance [54], suggesting that the (101) crystal plane can accelerate the OER process. Meanwhile, due to the formation of 3-D electron conduction interpenetrating networks by the strong coupling between the coexistence NRs, NWs and CNTs, the MnO_2-NWRs/$CNTs_{350}$ catalyst exhibits low binding energy, thus confirming the migration of the electron cloud. The migration of the electron cloud and the improvement of the valence state also promote the rate-determining step [33].

For SCs, the change of the MnO_2 structure and morphology give rise to significant change in the electronic, ionic conductivity, surface area and even the valence state, thereby further affecting the capacitance behavior of the material [56]. The 3-D electron conduction interpenetrating networks and flexible NWs can significantly enhance the pseudocapacitance of MnO_2/$CNTs_{350}$ by accelerating reversible redox transitions, including the transitions between Mn^{II}/Mn^{III} and Mn^{III}/Mn^{IV} species, as well as the exchange of cations and/or protons with the electrolyte [7]. It is thus evident that the excellent conductivity and abundance of electron pairs induced by the 3-D electron conduction interpenetrating networks can facilitate the performance of ORR/OER and SC [42,43,54].

4. Conclusions

In summary, a high efficient multifunctional MnO_2/CNTs catalyst with a robust and flexible morphology and unique 3-D electron conduction interpenetrating networks was synthesized using a two-step hydrothermal method through a facile and scalable strategy. The interweaving between MnO_2 nanowires (MWs)/nanorods(NRs) and carbon nanotubes renders the materials robust and flexible. The high activity and large specific capacitance of the MnO_2-NWRs/$CNTs_{350}$ material are induced by the strong coupling and synergistic effect between MnO_2-NWRs and CNTs, the coexistence of NRs/NWs and the existence of favorable crystal planes. The primary batteries with the MnO_2-NWRs/$CNTs_{350}$ cathode display high power densities (640 mW cm^{-2} for MABs and 400 mW cm^{-2} for ZABs) and specific capacities (1647 mA h g^{-1} for MABs and 781 mA h g^{-1} for ZABs), and outperform those with Pt/C cathode. The rechargeable ZAB with the MnO_2-NWRs/$CNTs_{350}$ cathode exhibits a high discharge voltage/extremely low charge voltage and excellent stability for up to 140 h, which is clearly superior to that with the Pt/C + IrO_2 cathode. Notably, the flexible rechargeable ZABs, MABs and SCs possess high power density, decent C-D stability and good capacitive characteristics due to the high-activity and flexible MnO_2-NWRs/$CNTs_{350}$ catalyst material. The interweaving between MnO_2-NWRs and CNTs makes the MnO_2-NWRs/$CNTs_{350}$ material more flexible and robust, thereby enhancing the possibility of its application in flexible devices.

Declaration of competing interest

The authors declare that they have no known competing financial interests or personal relationships that could have appeared to influence the work reported in this paper.

CRediT authorship contribution statement

Nengneng Xu: Conceptualization, Methodology, Investigation, Formal analysis, Writing - original draft, Writing - review & editing. **Jiawen Liu:** Validation, Data curation, Investigation, Writing - original draft, Writing - review & editing. **Jinli Qiao:** Conceptualization, Methodology, Funding acquisition, Project administration, Resources, Supervision, Validation, Writing - review & editing. **Haitao Huang:** Conceptualization, Visualization, Writing - original draft, Writing - review & editing. **Xiao-Dong Zhou:** Data curation, Funding acquisition, Project administration, Supervision, Writing - review & editing.

Acknowledgments

The authors appreciate supports from National Natural Science Foundation of China (21972017), the “Scientific and Technical Innovation Action Plan” Hong Kong, Macao and Taiwan Science &Technology Cooperation Project of Shanghai Science and Technology Committee (19160760600) and the U.S. National Science Foundational (NSF-1747603).

Appendix A. Supplementary data

Supplementary data to this article can be found online at https://doi.org/10.1016/j.jpowsour.2020.227992.

References

[1] D. Gu, Y. Zhou, R. Ma, F. Wang, Q. Liu, J. Wang, Nano-Micro Lett. 10 (2018) 29.
[2] D. Zhou, Z. Cai, X. Lei, W. Tian, Y. Bi, Y. Jia, N. Han, T. Gao, Q. Zhang, Y. Kuang, J. Pan, X. Sun, X. Duan, Adv. Energy Mater. 8 (2018), 1701905.
[3] J. Pan, X.L. Tian, S. Zaman, Z. Dong, H. Liu, H.S. Park, B.Y. Xia, Batter. Supercaps 2 (2018) 336–347.
[4] C. Han, W. Li, H.-K. Liu, S. Dou, J. Wang, Mater. Horiz. 6 (2019) 1812–1827.
[5] F. Cheng, J. Chen, Chem. Soc. Rev. 41 (2012) 2172–2192.
[6] Y. Li, H. Dai, Chem. Soc. Rev. 43 (2014) 5257–5275.
[7] G. Wang, L. Zhang, J. Zhang, Chem. Soc. Rev. 41 (2012) 797–828.
[8] R.A. Senthil, J. Pan, X. Yang, Y. Sun, Int. J. Hydrogen Energy 43 (2018) 21824–21834.
[9] Y. Sun, S. Guo, W. Li, J. Pan, C. Fernandez, R.A. Senthil, X. Sun, J. Power Sources 405 (2018) 80–88.
[10] J. Fu, J. Zhang, X. Song, H. Zarrin, X. Tian, J. Qiao, L. Rasen, K. Li, Z. Chen, Energy Environ. Sci. 9 (2016) 663–670.
[11] X. Chen, B. Liu, C. Zhong, Z. Liu, J. Liu, L. Ma, Y. Deng, X. Han, T. Wu, W. Hu, J. Lu, Adv. Energy Mater. 7 (2017), 1700779.
[12] N. Xu, X. Li, H. Li, Y. Wei, J. Qiao, Sci. Bull. 62 (2017) 1216–1226.
[13] P. Wang, Y. Lin, L. Wan, B. Wang, ACS Appl. Mater. Interfaces 11 (2019) 37701–37707.
[14] N. Zhao, F. Wu, Y. Xing, W. Qu, N. Chen, Y. Shang, M. Yan, Y. Li, L. Li, R. Chen, ACS Appl. Mater. Interfaces 11 (2019) 15537–15542.
[15] C.-S. Li, Y. Sun, F. Gebert, S.-L. Chou, Adv. Energy Mater. 7 (2017), 1700869.
[16] Z.X. Zhang, Z.F. Li, C.Y. Sun, T.W. Zhang, S.W. Wang, Catal. Today 298 (2017) 241–249.
[17] M.M. Sk, C.Y. Yue, K. Ghosh, R.K. Jena, J. Power Sources 308 (2016) 121–140.
[18] A. González, E. Goikolea, J.A. Barrena, R. Mysyk, Renew. Sustain. Energy Rev. 58 (2016) 1189–1206.
[19] S. Osman, R.A. Senthil, J. Pan, Y. Sun, J. Power Sources 414 (2019) 401–411.
[20] A. Khan, R.A. Senthil, J. Pan, Y. Sun, J. Electrochem. Soc. 166 (2019) A2273–A2279.
[21] X. Liu, M. Park, M.G. Kim, S. Gupta, G. Wu, J. Cho, Angew. Chem. 54 (2015) 9654–9658.
[22] J. Fu, Z.P. Cano, M.G. Park, A. Yu, M. Fowler, Z. Chen, Adv. Mater. 29 (2017), 1604685.
[23] T.Y. Ma, S. Dai, M. Jaroniec, S.Z. Qiao, J. Am. Chem. Soc. 136 (2014) 13925–13931.

[24] S.K. Bikkarolla, F.J. Yu, W.Z. Zhou, P. Joseph, P. Cumpson, P. Papakonstantinou, J. Mater. Chem. A 2 (2014) 14493–14501.
[25] P. Tan, B. Chen, H. Xu, H. Zhang, W. Cai, M. Ni, M. Liu, Z. Shao, Energy Environ. Sci. 10 (2017) 2056–2080.
[26] S.W. Donne, A.F. Hollenkamp, B.C. Jones, J. Power Sources 195 (2010) 367–373.
[27] C. Li, X. Han, F. Cheng, Y. Hu, C. Chen, J. Chen, Nat. Commun. 6 (2015) 7345.
[28] Y. Yuan, C. Zhan, K. He, H. Chen, W. Yao, S. Sharifi-Asl, B. Song, Z. Yang, A. Nie, X. Luo, H. Wang, S.M. Wood, K. Amine, M.S. Islam, J. Lu, R. Shahbazian-Yassar, Nat. Commun. 7 (2016), 13374.
[29] H.L. Fan, F. Ran, X.X. Zhang, H.M. Song, X.Q. Niu, L.B. Kong, L. Kang, Nano-Micro Lett. 7 (2015) 59–67.
[30] Z. Qi, A. Younis, D. Chu, S. Li, Nano-Micro Lett. 8 (2016) 165–173.
[31] H. Ma, B. Wang, RSC Adv. 4 (2014) 46084–46092.
[32] F. Meng, H. Zhong, D. Bao, J. Yan, X. Zhang, J. Am. Chem. Soc. 138 (2016) 10226–10231.
[33] S. Lee, G. Nam, J. Sun, J.S. Lee, H.W. Lee, W. Chen, J. Cho, Y. Cui, Angew. Chem. 55 (2016) 8599–8604.
[34] P.-C. Li, C.-C. Hu, T.-C. Lee, W.-S. Chang, T.H. Wang, J. Power Sources 269 (2014) 88–97.
[35] A. Débart, A.J. Paterson, J. Bao, P.G. Bruce, Angew. Chem. 120 (2008) 4597–4600.
[36] K. Selvakumar, S.M. Senthil Kumar, R. Thangamuthu, G. Kruthika, P. Murugan, Int. J. Hydrogen Energy 39 (2014) 21024–21036.
[37] M.S. Wu, Appl. Phys. Lett. 87 (2005).
[38] R. Cao, J.-S. Lee, M. Liu, J. Cho, Adv. Energy Mater. 2 (2012) 816–829.
[39] D.U. Lee, P. Xu, Z.P. Cano, A.G. Kashkooli, M.G. Park, Z. Chen, J. Mater. Chem. A 4 (2016) 7107–7134.
[40] Y.L. Cao, H.X. Yang, X.P. Ai, L.F. Xiao, J. Electroanal. Chem. 557 (2003) 127–134.
[41] S. Devaraj, N. Munichandraiah, J. Phys. Chem. C 112 (2008) 4406–4417.
[42] Y. Yuan, S.M. Wood, K. He, W. Yao, D. Tompsett, J. Lu, A. Nie, M.S. Islam, R. Shahbazian-Yassar, ACS Nano 10 (2016) 539–548.
[43] D.A. Tompsett, S.C. Parker, M.S. Islam, J. Am. Chem. Soc. 136 (2014) 1418–1426.
[44] J.S. Lee, G.S. Park, H.I. Lee, S.T. Kim, R. Cao, M. Liu, J. Cho, Nano Lett. 11 (2011) 5362–5366.
[45] Z. Chen, A. Yu, R. Ahmed, H. Wang, H. Li, Z. Chen, Electrochim. Acta 69 (2012) 295–300.
[46] H. Su, X.-T. Wang, J.-X. Hu, T. Ouyang, K. Xiao, Z.-Q. Liu, J. Mater. Chem. A 7 (2019) 22307–22313.
[47] J. Yang, X. Wang, B. Li, L. Ma, L. Shi, Y.J. Xiong, H.X. Xu, Adv. Funct. Mater. 27 (2017).
[48] P. Yue, Z. Li, S. Wang, Y. Wang, Int. J. Hydrogen Energy 40 (2015) 6809–6817.
[49] I. Roche, E. Chainet, M. Chatenet, J. Vondrak, J. Phys. Chem. C 111 (2007) 1434–1443.
[50] B. Sambandam, V. Soundharrajan, S. Kim, M.H. Alfaruqi, J. Jo, S. Kim, V. Mathew, Y.-k. Sun, J. Kim, J. Mater. Chem. A 6 (2018) 3850–3856.
[51] M. Kang, E.D. Park, J.M. Kim, J.E. Yie, Appl. Catal. A Gen. 327 (2007) 261–269.
[52] F. Larachi, J. Pierre, A. Adnot, A. Bernis, Appl. Surf. Sci. 195 (2002) 236–250.
[53] Q.W. Tang, L.H. Jiang, J. Liu, S.L. Wang, G.Q. Sun, ACS Catal. 4 (2014) 457–463.
[54] V. Tripkovic, H.A. Hansen, T. Vegge, ChemSusChem 11 (2018) 629–637.
[55] N. Xu, Y. Liu, X. Zhang, X. Li, A. Li, J. Qiao, J. Zhang, Sci. Rep. 6 (2016), 33590.
[56] L. Li, X.H. Feng, Y. Nie, S.G. Chen, F. Shi, K. Xiong, W. Ding, X.Q. Qi, J.S. Hu, Z. D. Wei, L.J. Wan, M.R. Xia, ACS Catal. 5 (2015) 4825–4832.
[57] S. Islam, M.H. Alfaruqi, V. Mathew, J. Song, S. Kim, S. Kim, J. Jo, J.P. Baboo, D. T. Pham, D.Y. Putro, Y.-K. Sun, J. Kim, J. Mater. Chem. A 5 (2017) 23299–23309.